



# High-crystalline and high-aspect-ratio hematite nanotube photoanode for efficient solar water splitting

Chenchen Feng<sup>a,b</sup>, Shurong Fu<sup>a,b</sup>, Wei Wang<sup>a,b</sup>, Yajun Zhang<sup>a</sup>, Yingpu Bi<sup>a,\*</sup>

<sup>a</sup> State Key Laboratory for Oxo Synthesis & Selective Oxidation, National Engineering Research Center for Fine Petrochemical Intermediates, Lanzhou Institute of Chemical Physics, CAS, Lanzhou 730000, China

<sup>b</sup> University of Chinese Academy of Sciences, Beijing 100049, China

## ARTICLE INFO

### Keywords:

Hematite  
Nanotube arrays  
High-temperature  
High aspect ratio  
Water oxidation

## ABSTRACT

Hematite ( $\alpha$ -Fe<sub>2</sub>O<sub>3</sub>) nanotube arrays with high aspect ratio and well-defined crystalline structures are highly attractive for photoelectrochemical water splitting. However, their design and fabrication remain a great challenge resulted from the poor thermal stability. Herein, we demonstrate that the high-crystalline Fe<sub>2</sub>O<sub>3</sub> nanotube arrays with average length of 2  $\mu$ m and high density of  $2.5 \times 10^7$  tubes/cm<sup>2</sup> could survive extended calcination temperatures up to  $\sim 800$  °C without any sintering. Owing to the well-oriented tubular structure, high light absorption and rich surface defects, this Fe<sub>2</sub>O<sub>3</sub> nanotube photoanode exhibits a significantly improved PEC activity for water oxidation, and the photocurrent could be achieved up to 1.2 mA cm<sup>-2</sup> at 1.23 V (vs. reversible hydrogen electrode, RHE). The decoration of FeOOH/NiOOH dual-cocatalysts not only caused a negative shift on onset-potential (170 mV), but also increased the photocurrent density up to 2.0 mA cm<sup>-2</sup> (1.23 V<sub>RHE</sub>), which is the highest value among the reported hematite nanotube photoanodes.

## 1. Introduction

Since the photoelectrochemical (PEC) water splitting on single-crystal TiO<sub>2</sub> photoanode has been firstly reported in 1972, it is still a great challenge to produce a stable and efficient material for converting solar energy into hydrogen fuels [1–8]. Hematite ( $\alpha$ -Fe<sub>2</sub>O<sub>3</sub>) is a promising candidate due to its favorable bandgap (2.1 eV), photo-stability, and abundance, which possesses a theoretical conversion efficiency of 12.9% for solar energy [9–14]. However, most reported PEC activities of Fe<sub>2</sub>O<sub>3</sub> photoanodes are far below its theoretical expectation, mainly suffering from the poor conductivity, short carrier diffusion length, and surface-trapping states [15–18]. More specifically, these limitations were mainly derived from the poor crystallinity of the as-prepared Fe<sub>2</sub>O<sub>3</sub> photoanodes [15,19]. It is well-known that high-temperature calcination ( $\geq 750$  °C) could effectively promote the crystallinity of hematite, which would effectively improve the electronic conductivity and facilitate charge transfer, as well as passivate the surface states [20,21]. However, the high temperature calcination of one-dimensional (1D) hematite nanoarrays, especially for hollow nanotubes, mostly resulted in the structural collapse and poor activities for PEC water oxidation [22,23].

To address these limitations, considerable efforts have focused on the introduction of templates to resist structural deformation, and a few

studies have been reported to fabricate the well-crystalline Fe<sub>2</sub>O<sub>3</sub> nanotube (NT) photoanodes under high temperature calcination. For example, the ZrO<sub>2</sub>-Fe<sub>2</sub>O<sub>3</sub> NT arrays could survive from the structural deformation during high-temperature calcination, and this nanotube photoanode showed an improved PEC water oxidation activity [24]. However, after high-temperature calcination, the length of Fe<sub>2</sub>O<sub>3</sub> NT has been greatly reduced ( $\leq 300$  nm), and the low density of nanotube arrays usually resulted in the significant decrease of light absorption. Thereby, the high-temperature fabrication of well-oriented and high-crystallized Fe<sub>2</sub>O<sub>3</sub> NT arrays with the high aspect ratios and dense structure is still a great challenge for PEC water splitting and other applications.

Here, we demonstrate the high-temperature fabrication of well-oriented Fe<sub>2</sub>O<sub>3</sub> NT arrays with the high density and average length of 2  $\mu$ m on Sb-SnO<sub>2</sub> substrate. More specifically, the high aspect ratios and high density can significantly enhance the solar light absorption, and high-crystalline structure can facilitate charge separation and transport and increase the number of surface active sites at the photoanode/electrolyte interface. As expected, this Fe<sub>2</sub>O<sub>3</sub> photoanode exhibits a highly improved PEC activity for water splitting. Furthermore, the photocurrent density could be further increased up to 2.0 mA cm<sup>-2</sup> at 1.23 V<sub>RHE</sub> with decorating FeOOH/NiOOH dual-cocatalysts. Additionally, an evident negative shift on onset potential for water oxidation as well

\* Corresponding author.

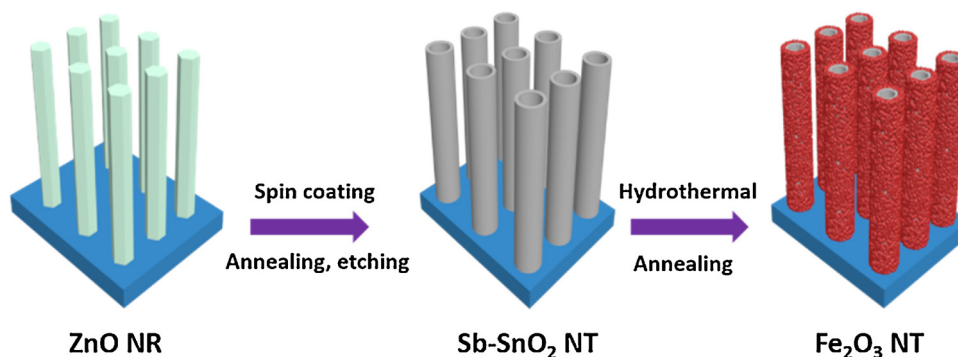
E-mail address: [yingpubi@licp.cas.cn](mailto:yingpubi@licp.cas.cn) (Y. Bi).

<https://doi.org/10.1016/j.apcatb.2019.117900>

Received 25 March 2019; Received in revised form 13 June 2019; Accepted 22 June 2019

Available online 24 June 2019

0926-3373/ © 2019 Elsevier B.V. All rights reserved.



Scheme 1. Illustration of the preparation of Fe<sub>2</sub>O<sub>3</sub> NT photoanodes.

as excellent PEC stability has also been achieved.

## 2. Results and discussion

Scheme 1 illustrates the typical synthetic process for Fe<sub>2</sub>O<sub>3</sub> NT arrays grown on Sb-SnO<sub>2</sub> conductive substrate. Briefly, Sb-SnO<sub>2</sub> nanorods were firstly prepared by using ZnO nanorod (NR) arrays as sacrifice-template [25]. Then, Fe<sub>2</sub>O<sub>3</sub> were in situ grown on the surface of Sb-SnO<sub>2</sub> NT via a hydrothermal process, finally annealed at high temperature (750 °C). Their morphology and structure changes under different growth stages were studied by scanning electron microscopy (SEM). Fig. 1A and B show the typical top and cross-section views of SEM images of ZnO NR arrays prepared via a seed-layer assisted growth process, clearly revealing that well-aligned nanorods with the diameter range from 100 to 150 nm were grown on FTO substrate. When the ZnO NR arrays were utilized as the growth template and subsequently removed by acid-treatment, the Sb-SnO<sub>2</sub> nanoarrays composed of 1D hollow structure with the rough surface have been obtained (Figure S1). The transmission electron microscopy (TEM) images (Figure S2) could further confirm the hollow tubular structure with a main wall-thickness of 30 nm. After the growth of FeOOH (Figure S3) and annealing at 750 °C, it can be clearly seen from SEM images (Fig. 1C and D) that except for the further increased diameters, no evident structural reconstruction can be observed. More specifically, these well-oriented Fe<sub>2</sub>O<sub>3</sub> NT nanoarrays have an average length of 2 μm and the density of  $2.5 \times 10^7$  tubes/cm<sup>2</sup>. Energy-dispersive spectroscopy (EDS) elemental mapping shows that the Fe, O, Sn and Sb elements are uniformly distributed in the whole detection-region (Fig. 2E–H and S4). High-resolution TEM (HR-TEM) images (Fig. 2I) clearly reveal that well-crystalline Fe<sub>2</sub>O<sub>3</sub> nanocrystals were compactly coated on the external surface of Sb-SnO<sub>2</sub> NT with a lattice spacing of 0.368 nm, which could be well indexed to the (012) crystal plane of α-Fe<sub>2</sub>O<sub>3</sub>. Moreover, an ultrathin disorder layer with the thickness about 0.5 nm has been uniformly formed on the surface of Fe<sub>2</sub>O<sub>3</sub> nanocrystals, which should be resulted from the formation of surface defect sites during high-temperature calcination. Moreover, the well-defined crystal boundary between Fe<sub>2</sub>O<sub>3</sub> and SnO<sub>2</sub> could be clearly observed in Fig. 2J, and the lattice spacing of 0.335 nm and 0.368 nm could be well indexed to the (110) plane of SnO<sub>2</sub> and (012) plane of Fe<sub>2</sub>O<sub>3</sub>, respectively. These demonstrations clearly reveal that the Fe<sub>2</sub>O<sub>3</sub> NT arrays with high crystallinity, large aspect ratio, and high density have been fabricated by the high-temperature calcination route.

The effect of annealing temperature on the crystallinity of Fe<sub>2</sub>O<sub>3</sub> NT arrays have been explored by X-ray diffraction (XRD). Fig. 2A shows the XRD patterns of Fe<sub>2</sub>O<sub>3</sub> annealed at 550 °C (Fe<sub>2</sub>O<sub>3</sub> NT-550) and 750 °C (Fe<sub>2</sub>O<sub>3</sub> NT-750), respectively, clearly revealing that except for SnO<sub>2</sub> from the substrate, all the diffraction peaks could be well indexed to the α-Fe<sub>2</sub>O<sub>3</sub> crystal structure (JCPDS NO. 33-0664). Moreover, it is worth noting that Fe<sub>2</sub>O<sub>3</sub> NT-750 exhibits much higher intensity of diffraction peaks than that of Fe<sub>2</sub>O<sub>3</sub> NT-550, clearly confirming that the high-

temperature calcination could effectively promote the crystallinity degree of Fe<sub>2</sub>O<sub>3</sub>. Their ultraviolet-visible diffuse reflectance spectra (Fig. 2B) reveal that although these two samples have a same spectral absorption edge ( $\lambda \leq 600$  nm), the absorption intensity of Fe<sub>2</sub>O<sub>3</sub> NT-750 is much higher than that of Fe<sub>2</sub>O<sub>3</sub> NT-550, suggesting that high crystallinity is favorable to improve the light-absorption capability. Based on the Kubelka-Munk function (Fig. 2C), the calculated bandgaps of Fe<sub>2</sub>O<sub>3</sub> NT-550 and Fe<sub>2</sub>O<sub>3</sub> NT-750 were 2.14 and 2.12 eV, respectively. Furthermore, Fig. 2D and S9 show the ultraviolet photoelectron spectroscopy (UPS) and X-ray photoelectron spectroscopy (XPS) valence band spectra. According to the literatures [26,27], the values of work function for Fe<sub>2</sub>O<sub>3</sub> NT-550 and Fe<sub>2</sub>O<sub>3</sub> NT-750 are 5.71 and 6.11 eV (vs. vacuum energy ( $E_{\text{vac}}$ )), respectively, the calculated valence band positions are 2.87 and 3.29 eV (vs. normal hydrogen electrode (NHE)). Combined with the value of bandgaps, the conduction band position of Fe<sub>2</sub>O<sub>3</sub> NT-550 and Fe<sub>2</sub>O<sub>3</sub> NT-750 are 0.73 and 1.17 eV (vs. NHE), clearly indicating that Fe<sub>2</sub>O<sub>3</sub> NT-750 exhibits more positive valence band position (Fig. 2E). Based on the HRTEM and XRD results, the atomic structure as well as defect sites for Fe<sub>2</sub>O<sub>3</sub> NT-550 and Fe<sub>2</sub>O<sub>3</sub> NT-750 samples has been proposed in Fig. 2E. The low temperature calcination leads to the poor crystal structure and bulk defects, which may induce the negative shift of valence band position. In contrast, owing to the well-defined crystallinity, the Fe<sub>2</sub>O<sub>3</sub> NT-750 possesses the regular atom structure with only surface defects, which facilitate the positive shift of valence band position. Based on above results, it was concluded that high-temperature calcination not only promotes the high crystallinity but also enhances the light absorption capacity of Fe<sub>2</sub>O<sub>3</sub>.

Furthermore, the surface chemical states of Fe<sub>2</sub>O<sub>3</sub> NT under various calcination temperatures have been explored by XPS (Fig. 3A and B). As compared with Fe<sub>2</sub>O<sub>3</sub> NT-550 sample, Fe<sub>2</sub>O<sub>3</sub> NT-750 exhibits stronger Fe<sup>2+</sup> peak (710.4 eV) and satellite peak (715.7 eV) in the Fe 2p core level spectra (Fig. 3A), resulting from the formation of surface defects (O<sub>v</sub>) during high-temperature calcination [28,29]. For the O 1s core level spectra (Fig. 3B), the peaks could be well fitted into three peaks, including lattice oxygen, vacancy oxygen, and hydroxyl oxygen, respectively [30,31]. Notably, the higher intensity as well as lower binding energy of O<sub>v</sub> peak (530.9 eV) for Fe<sub>2</sub>O<sub>3</sub> NT-750 further confirms the abundant oxygen vacancies at the surface. To further explore the effect of calcination temperature on the surface active sites, the electrochemical surface areas (ECSAs) of Fe<sub>2</sub>O<sub>3</sub> NT-550 and Fe<sub>2</sub>O<sub>3</sub> NT-750 were measured in 1 M KOH (Figure S11) [32]. As shown in Fig. 3C, the Fe<sub>2</sub>O<sub>3</sub> NT-750 exhibits a much higher ECSA of 0.3 m F cm<sup>-2</sup> than that of Fe<sub>2</sub>O<sub>3</sub> NT-550 (0.14 m F cm<sup>-2</sup>), confirming that more active sites have been generated via high-temperature calcination. Furthermore, the linear sweep voltammetry (LSV) was performed to evaluate the oxygen evolution performance (Fig. 3D). Compared with Fe<sub>2</sub>O<sub>3</sub> NT-550, a rapidly increased current density has been achieved on Fe<sub>2</sub>O<sub>3</sub> NT-750 sample, which exhibits more efficient OER activities for water oxidation and is consistent with the more positive of valence band position.

The PEC activities for water splitting have been explored in 1 M

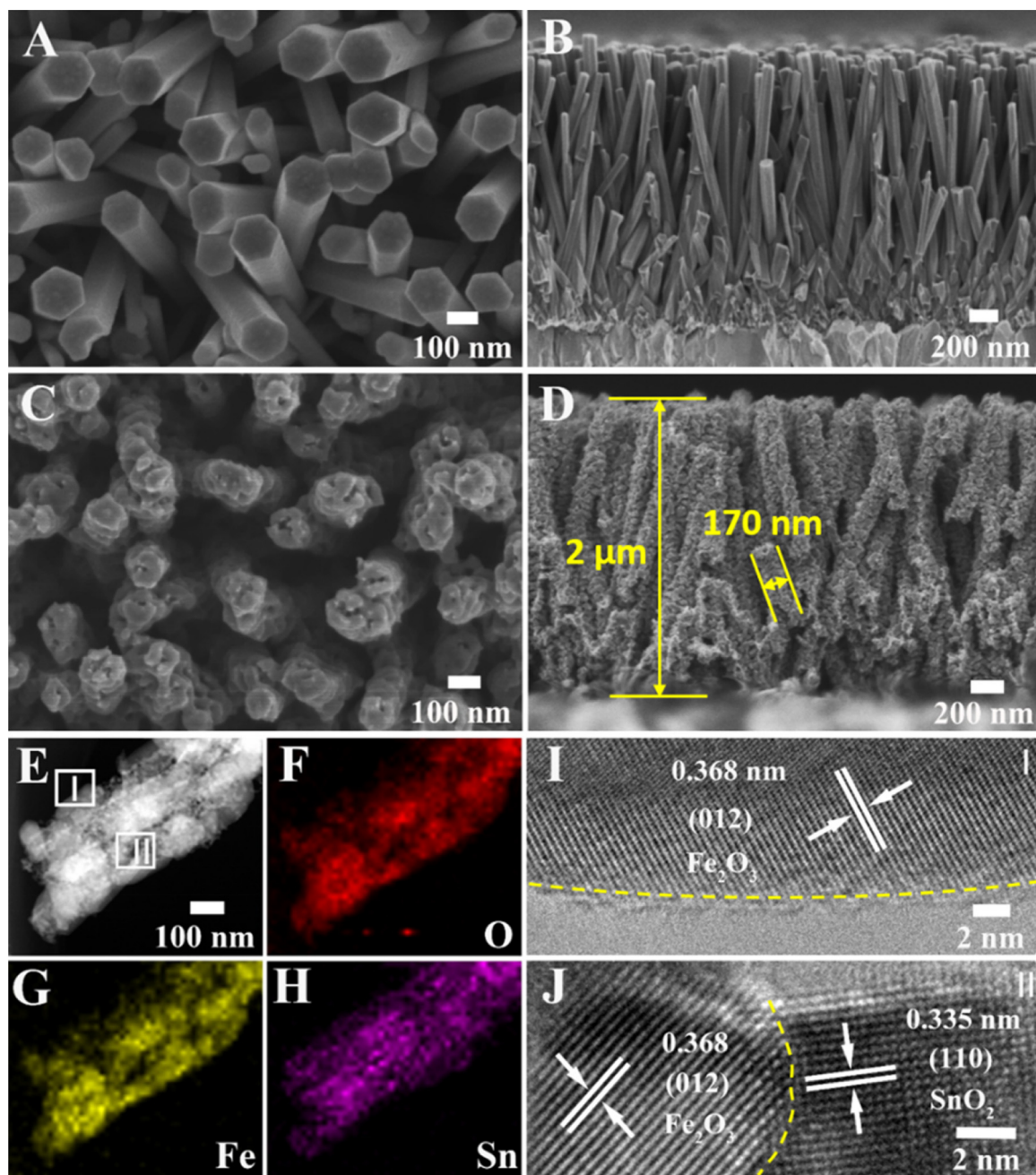


**Fig. 1.** Top and cross-sectional SEM images of ZnO NR (A, B) and  $\text{Fe}_2\text{O}_3$  NT arrays (C, D). (E) Bright-field image of  $\text{Fe}_2\text{O}_3$  NT and corresponding EDS elemental mapping for (F) O, (G) Fe, (H) Sn, respectively. HRTEM (I, J) images of  $\text{Fe}_2\text{O}_3$  NT as marked in (E).

KOH electrolyte under simulated solar light irradiation (AM 1.5 G,  $100 \text{ mW cm}^{-2}$ ). Fig. 4A shows the typical LSV curves, clearly revealing that the calcination temperature plays a crucial role in determining the PEC performance of  $\text{Fe}_2\text{O}_3$  NT photoanodes. More specifically, the  $\text{Fe}_2\text{O}_3$  NT-550 photoanode exhibits a relatively low photocurrent density about  $0.4 \text{ mA cm}^{-2}$  at  $1.23 V_{\text{RHE}}$ . Interestingly, with increasing the calcination temperature up to  $750^\circ\text{C}$ , the photocurrent density of  $\text{Fe}_2\text{O}_3$  NT-750 have been significantly increased up to  $1.2 \text{ mA cm}^{-2}$ , accompanied by a noticeable cathodic shift ( $\sim 100 \text{ mV}$ ) of onset potential. Moreover, Fig. 4B shows the incident photon-to-current conversion efficiency (IPCE) to evaluate their photoelectric conversion capabilities. At  $350 \text{ nm}$ , the  $\text{Fe}_2\text{O}_3$  NT-750 photoanode exhibits the much higher IPCE value (39%) than  $\text{Fe}_2\text{O}_3$  NT-550 photoanode (14%), which should be attributed to the enhanced light-absorption capability. In addition, the interfacial water oxidation kinetics was evaluated by

electrochemical impedance spectroscopy (EIS), and the charge transfer resistance is presented by the arcs in the Nyquist plots [33]. As shown in Fig. 4C,  $\text{Fe}_2\text{O}_3$  NT-750 exhibits a much smaller arc radius as well as lower interfacial charge transfer resistance ( $R_{\text{ct}} = 173.7 \Omega$ , Table S1) than that of  $\text{Fe}_2\text{O}_3$  NT-550 sample. Simultaneously, in Figure S14,  $\text{Fe}_2\text{O}_3$  NT-750 shows nearly an order of magnitude improvement for the carrier density ( $1.5 \times 10^{19} \text{ cm}^{-3}$ ) relative to the  $\text{Fe}_2\text{O}_3$  NT-550 ( $1.9 \times 10^{18} \text{ cm}^{-3}$ ). Based on above results, it is clear that the high-temperature calcination could dramatically improve the PEC performances for water oxidation.

Except for the high-crystallinity, the nanotube arrays with high aspect ratio and well-orientations should also be crucial for promoting the PEC performances. For comparison, the traditional  $\text{Fe}_2\text{O}_3$  nanoparticle (NP) photoanodes annealed at  $750^\circ\text{C}$  have also been prepared and tested under the same conditions. In Fig. 4D, it can be clearly seen that



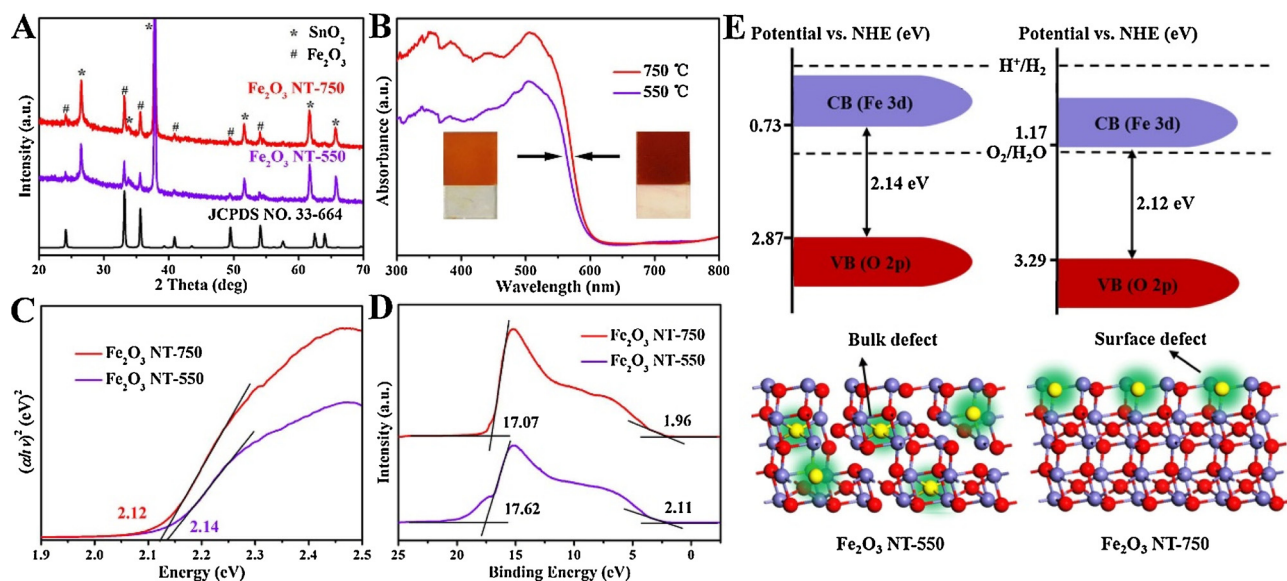


Fig. 2. (A) XRD patterns. (B) UV-vis diffuse reflectance spectra and (C) plot of the transformed KM function from the diffuse reflectance spectra. (D) UPS spectra of Fe<sub>2</sub>O<sub>3</sub> NT-550 and Fe<sub>2</sub>O<sub>3</sub> NT-750. (E) Band structure alignment and the schematic illustration of crystal structure of the two samples.

this nanoparticle photoanode only exhibits a photocurrent density of  $0.3 \text{ mA cm}^{-2}$  at  $1.23 V_{\text{RHE}}$ , which is much lower than the well-oriented nanotube photoanode ( $1.2 \text{ mA cm}^{-2}$ ), confirming the crucial roles of well-oriented nanotube structure for the remarkably improved PEC performance. On the other hand, the effects of surface oxygen vacancies on the PEC performances have also been studied by a facile in situ oxidation method. As shown in Figure S15, with increasing the oxidation time in the presence of H<sub>2</sub>O<sub>2</sub> aqueous solution, the photocurrent density of Fe<sub>2</sub>O<sub>3</sub> NT-750 photoanodes have gradually decreased from  $1.2 \text{ mA cm}^{-2}$  to  $0.7 \text{ mA cm}^{-2}$  at  $1.23 V_{\text{RHE}}$ . The abundant surface oxygen vacancies on Fe<sub>2</sub>O<sub>3</sub> NT-750 could serve as the active sites for improving the carrier transfer efficiency as well as oxygen evolution reactivity. On the basis of above results, it was considered that the

Fe<sub>2</sub>O<sub>3</sub> NT photoanodes with high aspect ratios and abundant surface-active sites could effectively enhance the light absorption capability and promote charge separation as well as transfer. Additionally, the hollow nanotube structure is promising to promote the hole transfer to surface active sites owing to the short diffusion length, while the electrons could be rapidly transferred via the inner Sb-SnO<sub>2</sub> nanolayers to the counter electrode for hydrogen generation. Thereby, owing to the spatial charge separation and transfer, this Fe<sub>2</sub>O<sub>3</sub> NT-750 exhibited the significant enhancement on the PEC activities for the solar water splitting.

To further promote oxygen evolution reaction kinetics, FeOOH/NiOOH dual-catalysts were modified on the Fe<sub>2</sub>O<sub>3</sub> NT-750 photoanodes. As shown in Fig. 4D, the Fe<sub>2</sub>O<sub>3</sub> NT-FeOOH/NiOOH photoanode

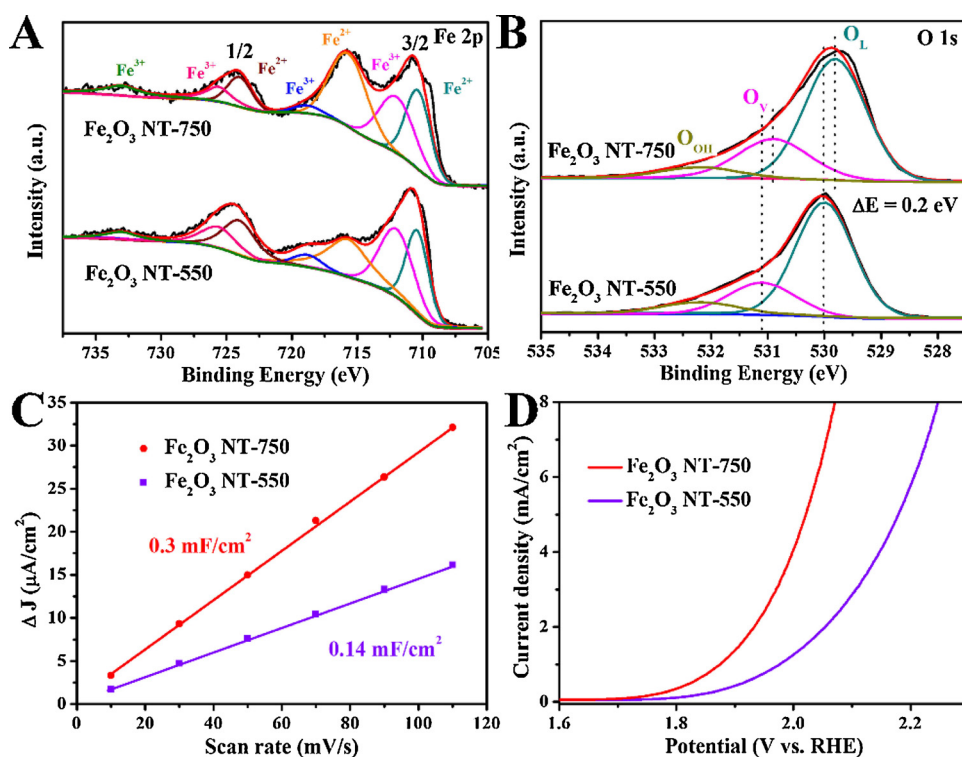
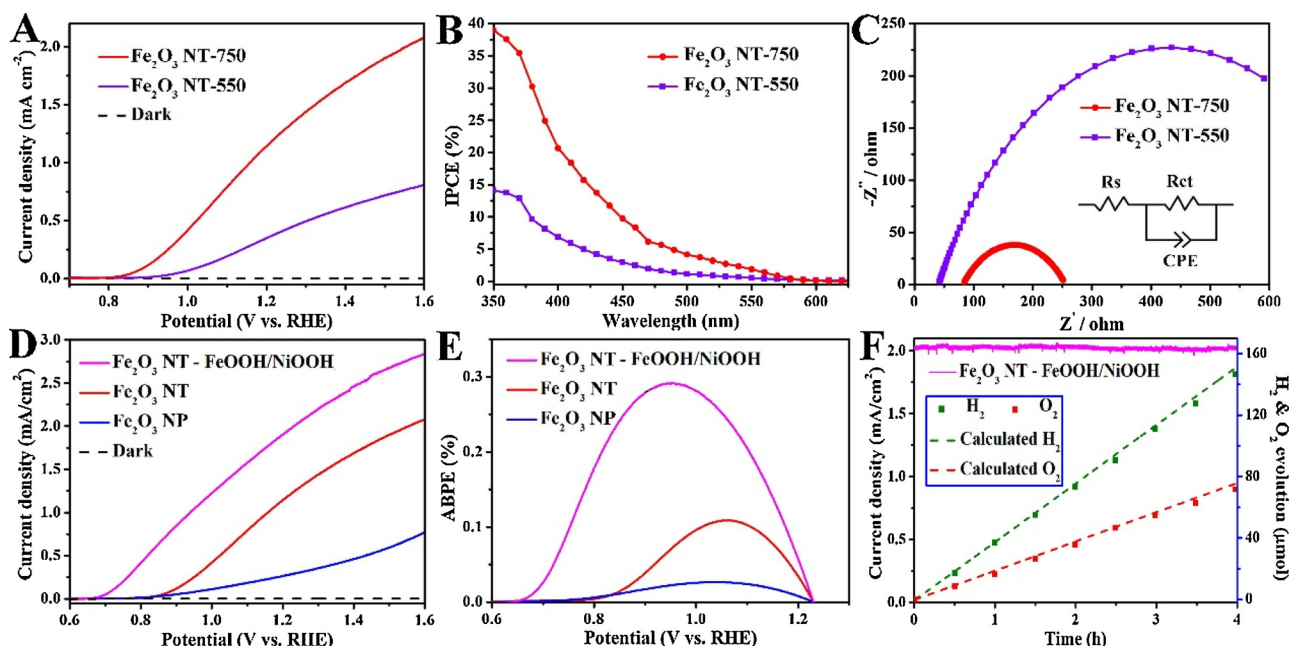


Fig. 3. (A, B) Fe 2p and O 1s XPS spectra of Fe<sub>2</sub>O<sub>3</sub> NT-550 and Fe<sub>2</sub>O<sub>3</sub> NT-750. Electrochemical properties of Fe<sub>2</sub>O<sub>3</sub> NT-550 and Fe<sub>2</sub>O<sub>3</sub> NT-750 were measured in 1 M KOH. (C) Charging current density differences plotted against scan rates. The linear slope, equivalent to twice of the double-layer capacitance ( $C_{\text{dl}}$ ), was used to represent the ECSA. (D) The OER performance at scan rate of 5 mV/s.



**Fig. 4.** (A) LSV, (B) IPCE and (C) EIS curves of the  $\text{Fe}_2\text{O}_3$  NT photoanodes under the different calcination temperature (550 °C and 750 °C). (D) LSV curves and (E) ABPE of  $\text{Fe}_2\text{O}_3$  NP,  $\text{Fe}_2\text{O}_3$  NT and  $\text{Fe}_2\text{O}_3$  NT-FeOOH/NiOOH photoelectrodes. (F) Photocurrent-time (J-t) curves and gas evolution for PEC water splitting of  $\text{Fe}_2\text{O}_3$  NT-FeOOH/NiOOH photoanode were performed at 1.23  $V_{\text{RHE}}$  under AM 1.5 G illumination in 1 M KOH electrolyte.

achieves a significantly improved photocurrent density of  $2.0 \text{ mA cm}^{-2}$  at 1.23  $V_{\text{RHE}}$ , accompanied by a further noticeable cathodic shift ( $\sim 170 \text{ mV}$ ) of onset potential. The applied bias photocurrent efficiencies (ABPE) shown in Fig. 4E clearly reveal that compared with the  $\text{Fe}_2\text{O}_3$  NP photoanodes with only an ABPE of 0.02% at 1.05  $V_{\text{RHE}}$ , a maximum ABPE value of 0.29% has been achieved for  $\text{Fe}_2\text{O}_3$  NT-FeOOH/NiOOH photoanode at 0.95  $V_{\text{RHE}}$ . Furthermore, the PEC stability of  $\text{Fe}_2\text{O}_3$  NT-FeOOH/NiOOH photoanodes was performed at 1.23  $V_{\text{RHE}}$ , and the photocurrent density could be well kept consistent during the test of 4 h (Fig. 4F), indicating its excellent photoelectric durability as well as structure stability for PEC water splitting. Furthermore, the corresponding  $\text{H}_2$  and  $\text{O}_2$  evolution were also measured by an online gas chromatography (GC). As shown in Fig. 4F, the produced  $\text{H}_2$  and  $\text{O}_2$  amounts are  $146 \mu\text{mol cm}^{-2}$  and  $71 \mu\text{mol cm}^{-2}$ , respectively, which are close to the theoretical calculated amounts of  $\text{H}_2$  and  $\text{O}_2$ . Accordingly, a Faradaic efficiency of  $\sim 96\%$  for water splitting has been obtained in this PEC device. On the other hand, the PEC performances of  $\text{Fe}_2\text{O}_3$  NT-FeOOH/NiOOH should be the highest among the reported hematite nanotube photoanodes.

### 3. Conclusion

In summary, the well-oriented and high crystalline  $\text{Fe}_2\text{O}_3$  NT arrays have been successfully synthesized by the high-temperature calcination, which exhibit significantly improved photocurrent density of  $1.2 \text{ mA cm}^{-2}$  at 1.23  $V_{\text{RHE}}$ . More specifically, the decoration of FeOOH/NiOOH cocatalyst could further improve charge separation efficiency and promote water oxidation kinetics, and a remarkable photocurrent density of  $2.0 \text{ mA cm}^{-2}$  at 1.23  $V_{\text{RHE}}$  has been achieved. Furthermore, the high crystallinity, efficient light absorption and surface defect sites resulted from the high-temperature calcination mainly attributed to the significantly improved PEC activity. These demonstrations may provide a feasible pathway for the high-temperature strategy to develop well-oriented nanotube photoanodes towards solar energy conversions.

### Declarations of interest

None.

### Acknowledgement

The work was supported by the National Natural Science Foundation of China (21832005, 21573264, 21622310, 21603247 and 21703266).

### Appendix A. Supplementary data

Supplementary material related to this article can be found, in the online version, at doi:<https://doi.org/10.1016/j.apcatb.2019.117900>.

### References

- [1] A. Fujishima, K. Honda, *Nature* 238 (1972) 37–38.
- [2] M. Grätzel, *Nature* 414 (2001) 338.
- [3] S. Choudhary, S. Upadhyay, P. Kumar, N. Singh, V.R. Satsangi, R. Shrivastav, S. Dass, *Int. J. Hydrogen Energy* 37 (2012) 18713–18730.
- [4] K. Sivula, R.V.D. Krol, *Nat. Rev. Mater.* 1 (2016) 15010.
- [5] C. Jiang, S.J.A. Moniz, A. Wang, T. Zhang, J. Tang, *Chem. Soc. Rev.* 46 (2017) 4645–4660.
- [6] J. Seo, H. Nishiyama, T. Yamada, K. Domen, *Angew. Chem. Int. Ed.* 57 (2018) 8396–8415.
- [7] T.T. Yao, X.R. An, H.X. Han, J.Q. Chen, C. Li, *Adv. Energy Mater.* 8 (21) (2018) 1800210.
- [8] Y. Yang, S.W. Niu, D.D. Han, T.Y. Liu, G.M. Wang, Y. Li, *Adv. Energy Mater.* 7 (19) (2017) 1700555.
- [9] O. Zandi, T.W. Hamann, *Nat. Chem.* 8 (2016) 778–783.
- [10] S.H. Shen, S.A. Lindley, X.Y. Chen, J.Z. Zhang, *Energy Environ. Sci.* 9 (2016) 2744–2775.
- [11] M. Forster, R.J. Potter, Y. Ling, Y. Yang, D.R. Klug, Y. Li, A.J. Cowan, *Chem. Sci.* 6 (2015) 4009–4016.
- [12] W. Li, D. He, S.W. Sheehan, Y.M. He, J.E. Thorne, X.H. Yao, G.W. Brudvig, D.W. Wang, *Energy Environ. Sci.* 9 (2016) 1794–1802.
- [13] C.W. Wang, S. Yang, W.Q. Fang, P. Liu, H.J. Zhao, H.G. Yang, *Nano Lett.* 16 (2016) 427–433.
- [14] K. Sivula, F. Le Formal, M. Grätzel, *ChemSusChem* 4 (2011) 432–449.
- [15] J.W. Jang, C. Du, Y.F. Ye, Y.J. Lin, X.H. Yao, J. Thorne, E. Liu, G. McMahon, J.F. Zhu, A. Javey, J.H. Guo, D.W. Wang, *Nat. Commun.* 6 (2015) 7447.
- [16] P. Peerakiatkhajohn, J.H. Yun, H.J. Chen, M.Q. Lyu, T. Tsuburee, L.Z. Wang, *Adv. Mater.* 28 (2016) 6405–6410.
- [17] G.D. Sabba, M.H. Kumar, L.H. Wong, J. Barber, M. Grätzel, N. Mathews, *Nano Lett.* 15 (2015) 3833–3839.
- [18] S.D. Tilley, M. Cornuz, K. Sivula, M. Grätzel, *Angew. Chem. Int. Ed.* 49 (2010) 6405–6408.
- [19] D.D. Qin, Y.L. Li, T. Wang, Y. Li, X.Q. Lu, J. Gu, Y.X. Zhao, Y.M. Song, C.L. Tao, *J. Mater. Chem. A* 3 (2015) 6751–6755.

- [20] Y.C. Ling, G.M. Wang, D.A. Wheeler, J.Z. Zhang, Y. Li, *Nano Lett.* 11 (2011) 2119–2125.
- [21] J.F. Han, X. Zong, Z.L. Wang, C. Li, *Phys. Chem. Chem. Phys.* 16 (2014) 23544–23548.
- [22] O. Zandi, T.W. Hamann, *J. Phys. Chem. Lett.* 5 (2014) 1522–1526.
- [23] K. Sivula, R. Zboril, F. Le Formal, R. Robert, A. Weidenkaff, J. Tucek, J. Frydrych, M. Grätzel, *J. Am. Chem. Soc.* 132 (2010) 7436–7444.
- [24] C.C. Li, A. Li, Z.B. Luo, J.J. Zhang, X.X. Chang, Z.Q. Huang, T. Wang, J.L. Gong, *Angew. Chem. Int. Ed.* 129 (2017) 4214–4219.
- [25] L. Zhou, Y. Yang, J. Zhang, P.M. Rao, *ACS Appl. Mater. Interfaces* 9 (2017) 11356–11362.
- [26] F. Li, J. Li, J. Zhang, L.L. Gao, X.F. Long, Y.P. Hu, S.W. Li, J. Jin, J.T. Ma, *ChemSusChem* 11 (2018) 1–10.
- [27] Y.L. Yang, S.C. Wang, Y.L. Jiao, Z.L. Wang, M. Xiao, A.J. Du, Y.L. Li, J.S. Wang, L.Z. Wang, *Adv. Funct. Mater.* 28 (2018) 1805698.
- [28] T.H. Jeona, A.D. Bokarea, D.S. Hanb, A. Abdel-Wahabb, H. Parkc, W. Choia, *Appl. Catal. B* 201 (2017) 591–599.
- [29] R. Zhang, Y.Y. Fang, T. Chen, F.L. Qu, Z.A. Liu, G. Du, A.M. Asiri, T. Gao, X.P. Sun, *ACS Sustain. Chem. Eng.* 5 (2017) 7502–7506.
- [30] C.Q. Zhu, C.L. Li, M.J. Zheng, J.J. Delaunay, *ACS Appl. Mater. Interfaces* 7 (2015) 22355–22363.
- [31] B.A. Sexton, A.E. Hughes, T.W. Turney, *J. Catal.* 97 (1986) 390–406.
- [32] L. Wang, B.B. Zhang, Q. Rui, *ACS Catal.* 8 (2018) 10564–10572.
- [33] S.C. Wang, P. Chen, J.H. Yun, Y.X. Hu, L.Z. Wang, *Angew. Chem. Int. Ed.* 56 (2017) 8500–8504.